M. Griebel, C. Rieger and P. Zaspel

Kernel-based stochastic collocation for the random two-phase Navier-Stokes equations

KERNEL-BASED STOCHASTIC COLLOCATION FOR THE RANDOM TWO-PHASE NAVIER–STOKES EQUATIONS

M. Griebel,[1,2] *C. Rieger,*[3] *& P. Zaspel*[4,*]

[1]*Institute for Numerical Simulation, Bonn University, Endenicher Allee 19b, D-53115 Bonn, Germany*

[2]*Fraunhofer Institute for Algorithms and Scientific Computing SCAI, Schloss Birlinghoven, D-53754 Sankt Augustin, Germany*

[3]*Department of Mathematics, RWTH Aachen University, Schinkelstr. 2, D-52062 Aachen, Germany*

[4]*Department of Mathematics and Computer Science, University of Basel, Spiegelgasse 1, 4051 Basel, Switzerland*

*Address all correspondence to: P. Zaspel, Department of Mathematics and Computer Science, University of Basel, Spiegelgasse 1, 4051 Basel, Switzerland, E-mail: peter.zaspel@unibas.ch

In this work, we apply stochastic collocation methods with radial kernel basis functions for an uncertainty quantification of the random incompressible two-phase Navier–Stokes equations. Our approach is nonintrusive and we use the existing fluid dynamics solver NaSt3DGPF to solve the incompressible two-phase Navier–Stokes equation for each given realization. We are able to empirically show that the resulting kernel-based stochastic collocation is highly competitive in this setting and even outperforms some other standard methods.

KEY WORDS: *stochastic collocation, incompressible two-phase Navier–Stokes, uncertainty quantification*

1. INTRODUCTION

In this paper, we apply uncertainty quantification to the large-scale complex fluid dynamics problem of incompressible two-phase flows modeled by the three-dimensional random two-phase Navier–Stokes equations. The two-phase Navier–Stokes equations describe the interaction of two nonmixing fluids like water and oil or water and air (at low Mach numbers). It has important applications ranging from fluvial construction analysis to flows in chemical bubble reactors. In fluvial construction analysis, a quantification of uncertainties is crucial for public safety. In chemical bubble column reactors, we can use uncertainty quantification to obtain a stochastic homogenization of the perturbation of a liquid in the presence of many rising bubbles. This is important for large-scale chemical process optimization.

Depending on the respective applications, we treat densities, viscosities, or volume forces as stochastic values or fields. This renders also the systems' solution, i.e., the velocity field, the pressure field, and the liquid-liquid interface as stochastic quantities. Moreover, quantities of interest computed from these solution fields thereby also become stochastic. After the numerical solution of the overall problem, its uncertainty quantification can be achieved by a stochastic moment analysis, which will include the evaluation of the, e.g., first stochastic moment. Methods for stochastic moment analysis are intrusive (e.g., stochastic Galerkin [1,2]) or nonintrusive (e.g., Monte Carlo, quasi-Monte Carlo [3], multilevel Monte Carlo [4] and (generalized) polynomial chaos [5] and stochastic collocation [6]). Moreover, there is some related work for stochastic moment analysis in computational fluid dynamics applications, with examples in groundwater flow [7] and incompressible flows [8,9]. However, to our knowledge, the application of the two-phase incompressible Navier–Stokes equations has never been considered before.

Our approach to solve the random two-phase Navier–Stokes equations will be based on a *nonintrusive stochastic collocation* approach. This enables us to reuse our existing two-phase Navier–Stokes solver NaSt3DGPF [10,11]. This code covers applications such as river simulations in the presence of hydraulic constructions and, more recently, sediment transport [12] and non-Newtonian flows [13]. It has also been parallelized on CPU and GPU clusters [14].

In stochastic collocation, spectral (sparse) tensor-product approximation [6] is widely used. However, since regularity results are in general not available for the two–phase Navier–Stokes equations, we can in general not expect to have the high parametric regularity required by some of the recent spectral approximation approaches (even in the regime of moderately high Reynolds numbers). Moreover, the number of samples in grid-based approximation approaches, even for sparse grids, can be prohibitively high due to its dyadic construction. This is problematic for our application, since already one single deterministic high-resolution two-phase Navier–Stokes simulation often requires computational resources in the range of hours to days on a parallel computer. Therefore, we introduce a mesh-free approach for the treatment of the stochastic variables, namely the radial basis function (RBF) kernel-based stochastic collocation, to achieve both high asymptotic convergence rates and good preasymptotic behavior for stochastic moment analysis. We note the close relationship of kernel-based approximation to kriging [15,16] with its low error for few collocation points and to Gaussian process regression [17] with its profound stochastic framework. Related recent work on kernel-based collocation covers the approximate solution of stochastic partial differential equations [18], the special case of an elliptic random PDE [19] by an intrusive method, the case of parametric partial differential equations [20], and the parallel treatment of large random partial differential equations; see [21].

In our numerical results with several rising bubble test cases, we focus on a small number of random parameters, which are of nearly equal importance to the simulation. This is justified by an engineering perspective where a few physical parameters are considered with small fluctuations. A small number of parameters is also justified by practical limitations since we would never be able to sample enough solutions (or store them) to sufficiently resolve a larger and higher-dimensional parameter domain. As discussed before, we do not assume or expect to have high spatial/temporal regularity for the quantities of interest. Therefore, we employ algebraically smooth kernels to this situation. Algebraically smooth kernels are known to achieve a convergence rate which corresponds to the minimum of the smoothness of the kernel and the smoothness of the function to be approximated; see [22]. Hence, by using a kernel approach with higher algebraic regularity, we employ a method which is capable of exploiting the unknown smoothness of the parametric function which needs to be reconstructed. Moreover, in the isotropic case where all dimensions in the parameter space are nearly equally important, we know that kernel methods are quasi-optimal; see [23]. From a practical point of view, kernel methods are easy to implement compared to more sophisticated approximation methods such as multilevel or sparse grid constructions. Finally, kernel methods allow one to increase the number of sampling points by just any arbitrary number and we do not need to stick to prime numbers (as in some QMC methods), grid sizes (as in some sparse grids), or dimensions of polynomial spaces. In addition, we use the Gaussian kernel if the quantity of interest might depend smoothly on the parameters as we expect it for integrated quantities of interest. In such a situation, kernel methods are able to provide exponential convergence rates from the very beginning. We confirm these statements by numerical results. In particular, we show empirically that kernel-based stochastic collocation methods allow one to outperform the algebraic convergence rates of isotropic (quasi-)Monte Carlo techniques. Moreover, in a direct comparison to a (sparse) spectral tensor-product method, in which we consider an integrated quantity of interest, the kernel-based method shows exponential convergence rates. Hence, our approach is able to deliver a decent approximation with very few deterministic solutions of the two-phase Navier–Stokes equations.

The remainder of this work is organized as follows. Section 2 introduces the random two-phase Navier–Stokes equations including details on their numerical treatment. Section 3 discusses the RBF kernel-based stochastic collocation. The main results, i.e., empirical convergence studies, are presented in Section 4. Finally, Section 5 gives some conclusions and a short outlook.

2. RANDOM TWO-PHASE NAVIER–STOKES EQUATIONS

The application problem motivating this work is a random version of the two-phase incompressible Navier–Stokes equations. They model the interaction of two incompressible fluids which do not mix but remain disjoint with a

common interface. Classical examples for such fluid-fluid systems in the real world are oil and water or water and air, noting that it is usual to assume air to be incompressible for the discussed test cases. The random model discussed here is derived from the deterministic two-phase Navier–Stokes equations as discussed, e.g., in [10]. Further references are [24,25].

Formally, the introduction of the random two-phase Navier–Stokes equations would start from a probability space (possibly infinite-dimensional) with stochastic parameters in which all stochastic variations are expressed. However, the finite-noise approximation leads us to consider only a D-dimensional parameter space $\mathcal{Y} \subset \mathbb{R}^D$, cf. e.g., [6]. The parameter space $\mathcal{Y}$ is considered to be a measure space $(\mathcal{Y}, \mathcal{B}, \rho\, d\mathbf{y})$ with density ρ and the usual Borel σ–algebra $\mathcal{B}$. Here we directly introduce the *finite-dimensional* (parametric) model of the random two-phase Navier–Stokes equations, noting that the parameter space $\mathcal{Y} \subset \mathbb{R}^D$ might be still high-dimensional, i.e., D might be large.

2.1 Finite-Dimensional Random Model

Now, we present the finite-dimensional random two-phase Navier–Stokes equations with respect to the parameter space $(\mathcal{Y}, \mathcal{B}, \rho\, d\mathbf{y})$. The physical space $\mathcal{D} \subset \mathbb{R}^3$ is a connected domain with boundary $\Gamma = \partial\mathcal{D}$. Two subdomains $\mathcal{D}_1, \mathcal{D}_2$ identify the two fluid phases. Technically, they are time- and parameter-dependent; i.e., $\mathcal{D}_i = \mathcal{D}_i(\mathbf{y}, t)$ for $i = 1, 2$ with $\mathcal{D}_1(\mathbf{y}, t) \cap \mathcal{D}_2(\mathbf{y}, t) = \emptyset$ for all $t \in [0, T]$ and $T \in \mathbb{R}_+$ the final simulation time. The full domain $\mathcal{D}$ is covered by $\mathcal{D}_1, \mathcal{D}_2$ and the time- and parameter-dependent fluid-fluid separation interface $\Gamma_f(\mathbf{y}, t)$. Thus there holds $\mathcal{D} = \mathcal{D}_1(\mathbf{y}, t) \cup \mathcal{D}_2(\mathbf{y}, t) \cup \Gamma_f(\mathbf{y}, t)$; cf. Fig. 1. Moreover, the outer domain boundary is decomposed into $\Gamma_1 := \Gamma \cap \partial\mathcal{D}_1$ and $\Gamma_2 := \Gamma \cap \partial\mathcal{D}_2$. We note that by this construction the whole domain $\mathcal{D}$ is fixed but the two subdomains and the free surface separating them are parameter-dependent. In each of the two subdomains $\mathcal{D}_i$, $i = 1, 2$, the finite-dimensional random system of the two-phase Navier–Stokes equations reads as

$$\rho_i(\mathbf{y})\frac{D\mathbf{u}_i}{Dt} = \nabla \cdot \mu_i(\mathbf{y})\mathbf{S}_i - \nabla p_i + \rho_i(\mathbf{y})\mathbf{g}(\mathbf{y}) \qquad \text{in} \quad \mathcal{Y} \times \mathcal{D}_i(\mathbf{y}) \times [0, T], \tag{1}$$

$$\nabla \cdot \mathbf{u}_i = 0 \qquad \text{in} \quad \mathcal{Y} \times \mathcal{D}_i(\mathbf{y}) \times [0, T], \tag{2}$$

$$\mathbf{u}_i = \mathbf{u}_{0_i}(\mathbf{y}, \mathbf{x}) \qquad \text{in} \quad \mathcal{Y} \times \mathcal{D}_i(\mathbf{y}) \times \{0\}, \tag{3}$$

$$\mathcal{B}\mathbf{u}_i = \mathbf{b}_\Gamma \qquad \text{on} \quad \mathcal{Y} \times \Gamma \times [0, T], \tag{4}$$

$$\frac{\partial p_i}{\partial \mathbf{n}_\Gamma} = 0 \qquad \text{on} \quad \mathcal{Y} \times \Gamma \times [0, T], \tag{5}$$

$$\mathbf{u}_1 = \mathbf{u}_2 \qquad \text{on} \quad \mathcal{Y} \times \Gamma_f(\mathbf{y}) \times [0, T], \tag{6}$$

$$[\mathbf{T}\mathbf{n}] = \sigma\kappa\mathbf{n} \qquad \text{on} \quad \mathcal{Y} \times \Gamma_f(\mathbf{y}) \times [0, T]. \tag{7}$$

The main part of the random two-phase Navier–Stokes equations is the momentum equation (1) and the continuity equation (2). The first equation is decomposed into the material derivative $D\mathbf{u}_i/Dt := \partial_t\mathbf{u}_i + (\mathbf{u}_i \cdot \nabla)\mathbf{u}_i$ and terms
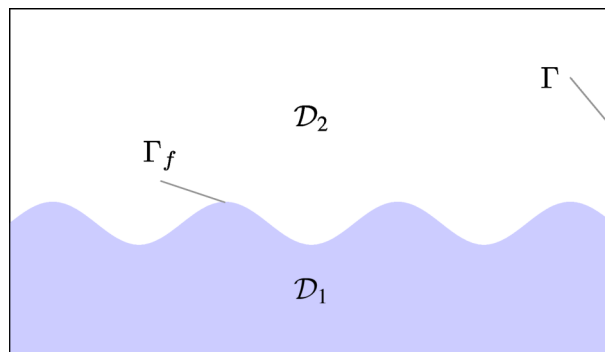

FIG. 1: The domain $\mathcal{D}$ with boundary Γ is subdivided into two distinct fluid phase domains $\mathcal{D}_1$ and $\mathcal{D}_2$ and the fluid-fluid interface Γ_f in the two-phase Navier–Stokes equations

involving the viscosity (with $\mathbf{S}_i := \nabla \mathbf{u}_i + \{\nabla \mathbf{u}_i\}^T$), pressure, and volume forces. The second equation represents the incompressibility constraint for both fluids.

Both fluids interact with respect to a random volume force $\mathbf{g} : \mathcal{Y} \times \mathcal{D} \to \mathbb{R}^3$, e.g., gravity with some perturbation.[†] At the fluid-fluid interface Γ_f, there holds the jump condition (7) for the stress tensor $\mathbf{T}_i := -p_i \mathbf{I} + \mu_i \mathbf{S}_i$, $\mathbf{T}_i : \mathcal{Y} \times \mathcal{D}_i \times [0,T] \to \mathbb{R}^{3 \times 3}$, with $[\mathbf{Tn}]$ being the jump $(\mathbf{T}_1 \mathbf{n} - \mathbf{T}_2 \mathbf{n})$ across the interface and $\mathbf{I} \in \mathbb{R}^{3 \times 3}$ being the identity matrix. The continuity condition for the velocities $\mathbf{u}_1$ and $\mathbf{u}_2$ at the interface is given in Eq. (6). Finally, $\sigma \in \mathbb{R}$ is the surface tension coefficient, $\kappa : \mathcal{Y} \times \Gamma_f(\mathbf{y}) \times [0,T] \to \mathbb{R}$ is the curvature of Γ_f, and $\mathbf{n} : \mathcal{Y} \times \Gamma_f(\mathbf{y}) \times [0,T] \to \mathbb{R}^3$ is the surface normal of the interface. For simplicity, we keep σ to be deterministic.

This system is augmented by proper initial conditions for the velocity field by $\mathbf{u}_{0_i} : \mathcal{D}_i \to \mathbb{R}^3$, by boundary conditions (4) for the velocities, and by approximate boundary conditions (5) for the pressures. Velocity boundary conditions are here denoted for the sake of simplicity by some general boundary operator $\mathcal{B}$ and the space-time-dependent right-hand side function $\mathbf{b}_\Gamma$. For all parameters $\mathbf{y} \in \mathcal{Y}$, Eqs. (1)–(7) are solved for the velocity fields $\mathbf{u}_i : \mathcal{Y} \times \mathcal{D}_i \times [0,T] \to \mathbb{R}^3$ [m/s] and pressures $p_i : \mathcal{Y} \times \mathcal{D}_i \times [0,T] \to \mathbb{R}$ [kg/(m·s²)]. The two important material properties for incompressible fluids are the (random) subdomain-wise constant densities $\rho_i : \mathcal{Y} \to \mathbb{R}$ [kg/m³] and viscosities $\mu_i : \mathcal{Y} \to \mathbb{R}$ [kg/(m·s)]. Note that it is common to have no initial conditions for the pressure, since the pressure is usually understood as a Lagrange multiplier. Moreover, the solution method applied in this work does not require initial conditions for pressure.

Altogether, this formulation of the random model explicitly introduces a parametric/random dependence of the two-phase Navier–Stokes equations in the densities, viscosities, the volume force, and the initial condition. This way, all other quantities become dependent on the random/parametric input.

2.2 Continuous Formulation Using Random Level Sets

We now follow the common approach to introduce a level-set function ϕ to distinguish the two fluid phases. For further details, see [10]. This way, the equations can be formulated with respect to the common domain $\mathcal{D}$. Deterministic level-set techniques have been proven useful in the context of two-phase flows in [24]. In our situation the level-set function ϕ is now random/parametric. To this end, $\phi : \mathcal{Y} \times \mathcal{D} \times [0,T] \to \mathbb{R}$ is a signed distance function implicitly defining the two random domains $\mathcal{D}_1, \mathcal{D}_2$ as

$$\phi(\mathbf{y}, \mathbf{x}, t) \begin{cases} < 0 & \text{if} \quad \mathbf{x} \in \mathcal{D}_1(\mathbf{y}, t), \\ = 0 & \text{if} \quad \mathbf{x} \in \Gamma_f(\mathbf{y}, t), \\ > 0 & \text{if} \quad \mathbf{x} \in \mathcal{D}_2(\mathbf{y}, t). \end{cases} \tag{8}$$

Also, ϕ obeys the eikonal equation

$$|\nabla_{\mathbf{x}} \phi(\mathbf{y}, \mathbf{x}, t)| = 1 \quad \text{for almost all} \quad (\mathbf{y}, \mathbf{x}, t) \in \mathcal{Y} \times \mathcal{D} \times [0,T], \tag{9}$$

which makes it for fixed parameter $\mathbf{y} \in \mathcal{Y}$ a distance function. The free surface Γ_f, i.e., the (random) interface between both fluids, is given by

$$\Gamma_f(\mathbf{y}, t) = \{\mathbf{x} : \phi(\mathbf{y}, \mathbf{x}, t) = 0\}. \tag{10}$$

Based on the continuum surface force scheme [26] it is possible to reformulate the discontinuous equation system (1)–(7) into a continuous representation [24]. This works analogously for the random/parametric case. In the remainder of this section, we understand all equations in the sense that they hold for (almost) every parameter value $\mathbf{y} \in \mathcal{Y}$. We here follow [10] and introduce, by slightly abusing notation, domain-dependent densities and viscosities,

$$\rho_\phi(\mathbf{y}) := \rho_1(\mathbf{y}) + (\rho_2(\mathbf{y}) - \rho_1(\mathbf{y})) H(\phi(\mathbf{y})), \tag{11}$$

$$\mu_\phi(\mathbf{y}) := \mu_1(\mathbf{y}) + (\mu_2(\mathbf{y}) - \mu_1(\mathbf{y})) H(\phi(\mathbf{y})), \tag{12}$$

[†] While a random volume force might not have an immediate physical correspondence, the choice of a random right-hand side in the literature on uncertainty quantification for model partial differential equations is very common. Therefore, this case is addressed here, too.

with the Heaviside step function,

$$H(\phi) := \begin{cases} 0 & \text{if} \quad \phi < 0, \\ \dfrac{1}{2} & \text{if} \quad \phi = 0, \\ 1 & \text{if} \quad \phi > 0. \end{cases} \tag{13}$$

This function is smoothed out in a neighborhood of the free surface leading to jump-free functions H^ϵ, ρ_ϕ^ϵ, and $\mu^\epsilon(\phi)$; cf. [10] for more details. It is then possible to derive the initial-boundary value problem,

$$\rho_\phi^\epsilon \frac{D\mathbf{u}}{Dt} = \nabla \cdot (\mu_\phi^\epsilon \mathbf{S}) - \nabla p - \sigma\kappa_\phi \delta^\epsilon \nabla\phi + \rho_\phi^\epsilon \mathbf{g} \qquad \text{in} \quad \mathcal{Y} \times \mathcal{D} \times [0, T], \tag{14}$$

$$\nabla \cdot \mathbf{u} = 0 \qquad \text{in} \quad \mathcal{Y} \times \mathcal{D} \times [0, T], \tag{15}$$

$$\partial_t \phi + \mathbf{u} \cdot \nabla\phi = 0 \qquad \text{in} \quad \mathcal{Y} \times \mathcal{D} \times [0, T], \tag{16}$$

$$|\nabla\phi| = 1 \qquad \text{on} \quad \mathcal{Y} \times \Gamma \times [0, T], \tag{17}$$

$$\mathbf{u} = \mathbf{u}_0 \qquad \text{in} \quad \mathcal{Y} \times \mathcal{D} \times \{0\}, \tag{18}$$

$$\mathcal{B}\mathbf{u} = \mathbf{b}_\Gamma \qquad \text{on} \quad \mathcal{Y} \times \Gamma \times [0, T], \tag{19}$$

$$\frac{\partial p}{\partial \mathbf{n}_\Gamma} = 0 \qquad \text{on} \quad \mathcal{Y} \times \Gamma \times [0, T], \tag{20}$$

$$\phi = \phi_0 \qquad \text{in} \quad \mathcal{Y} \times \mathcal{D} \times \{0\}, \tag{21}$$

$$\frac{\partial \phi}{\partial \mathbf{n}_\Gamma} = 0 \qquad \text{on} \quad \mathcal{Y} \times \Gamma \times [0, T], \tag{22}$$

with $\mathbf{u} : \mathcal{Y} \times \mathcal{D} \times [0, T] \to \mathbb{R}^3$ and $p : \mathcal{Y} \times \mathcal{D} \times [0, T] \to \mathbb{R}$ the velocity and pressure fields, respectively, defined on the full domain $\mathcal{D}$. It turns out that the jump condition for the stress tensor translates to the volume force $-\sigma\kappa_\phi \delta_\phi^\epsilon \nabla\phi$, where δ_ϕ^ϵ denotes a smoothed-out Dirac functional and κ_ϕ is the curvature of the free surface. It is given in the level-set case (cf. [27]) as

$$\kappa_\phi(\mathbf{y}, \mathbf{x}, t) = \nabla_\mathbf{x} \cdot \frac{\nabla_\mathbf{x}\phi(\mathbf{y}, \mathbf{x}, t)}{\|\nabla_\mathbf{x}\phi(\mathbf{y}, \mathbf{x}, t)\|} \quad \text{for } \mathbf{x} \in \Gamma_f(\mathbf{y}, t). \tag{23}$$

The transport equation (16) governs the evolution of the interface. Equation (17) describes the reinitialization of the level-set function and introduces a nonlinearity. It will be treated by an iterative method; see [10] for further details. Again, the system is augmented by proper initial and boundary conditions; see Eqs. (18)–(22). Altogether, the Eqs. (14)–(22) describe a continuum surface force formulation of the parametric Navier–Stokes equation. As already mentioned, this system of equations holds (in the sense of almost everywhere) for each parameter. For a fixed parameter, the system of equations reduces to a common deterministic two-phase Navier–Stokes equation.

2.3 Numerical Treatment of the Two-Phase Navier–Stokes Equations

The stochastic collocation approach only requires us to consider the solution of the deterministic two-phase Navier–Stokes equations for a set of fixed parameter values $\mathbf{y} \in \mathcal{Y}$. To this end, classical solution techniques can be used. In practice, we employ the flow solver NaSt3DGPF [10,11], which implements the pressure correction approach [28] to solve the deterministic two-phase Navier–Stokes equations over time. Details can be found in [10]. The main features of the code are as follows:

Finite differences/volumes are used as discretization method in space with a classical marker-and-cell (MAC) staggered uniform grid. The velocity components are therefore discretized on the centers of the cell faces whereas pressure and level-set function are discretized on the centers of the cells. Wherever it is necessary to evaluate quantities, e.g., from cell centers on the cell faces, higher-order interpolation is used. The convective terms of the momentum equations are discretized by the fifth-order weighted essentially nonoscillatory (WENO) scheme. The diffusion term is computed by second-order central differences. The WENO scheme is also applied to the gradient evaluation in

the reinitialization equation and to the transport term in the level-set advection. The pressure Poisson equation is discretized with a standard seven-point second order stencil and solved with a Jacobi-preconditioned conjugate gradient (CG) method. As time integrator, a second-order Adams–Bashforth scheme with an adaptive time step selection mechanism is employed, cf. [11], which obeys the Courant–Friedrichs–Lewy (CFL) condition.

As a consequence of this discretization and the numerical solution, note that we have at no point of our stochastic collocation procedure access to the true solutions $\mathbf{u}$, p, and ϕ. Instead, we will restrict ourselves to the numerical approximations $\mathbf{u}^h$, p^h, and ϕ^h where h indicates spatial and temporal discretization.

3. KERNEL-BASED STOCHASTIC COLLOCATION FOR STOCHASTIC MOMENT ANALYSIS

3.1 Objective

The numerical solution to the random two-phase Navier–Stokes system with random level sets consists of three components, namely a time-dependent velocity random vector field $\mathbf{u}^h : \mathcal{Y} \times \bar{\mathcal{D}} \times [0, T] \to \mathbb{R}^3$ with $\mathbf{u}^h = (u_1^h, u_2^h, u_3^h)^T$, and time-dependent pressure random field $p^h : \mathcal{Y} \times \bar{\mathcal{D}} \times [0, T] \to \mathbb{R}$ and time-dependent random domains $\mathcal{D}_i^h(\mathbf{y}, t)$ for $i = 1, 2$, which we represent by the time-dependent level-set random field $\phi^h : \mathcal{Y} \times \bar{\mathcal{D}} \times [0, T] \to \mathbb{R}$.

It is common not to consider the full solution but some *quantities of interest*, which are to be derived from these numerical solutions. To this end, we consider the following two quantities of interest. The first one is just the first component of the solution velocity field,

$$u_1^h : \mathcal{Y} \times \bar{\mathcal{D}} \times [0, T] \to \mathbb{R}. \tag{24}$$

This is a parameter-dependent real-valued field discretized in space and time. The second quantity of interest is the center of mass,

$$\mathbf{c}^h : \mathcal{Y} \times [0, T] \to \mathbb{R}^3, \tag{25}$$

with $\mathbf{c}^h := (c_1^h, c_2^h, c_3^h)^\top$ of the second fluid phase and

$$\mathbf{c}^h(\mathbf{y}, t) := \frac{1}{\mathrm{Vol}(\mathcal{D}_2^h(\mathbf{y}, t))} \int_{\mathcal{D}_2^h(\mathbf{y}, t)} \mathbf{x} \, d\mathbf{x} = \left(\int_{\mathcal{D}_2^h(\mathbf{y}, t)} 1 \, d\mathbf{x} \right)^{-1} \int_{\mathcal{D}_2^h(\mathbf{y}, t)} \mathbf{x} \, d\mathbf{x}. \tag{26}$$

Obviously, this is a vector-valued parameter-dependent quantity in time. We will here only focus on the second component, namely c_2^h.

For both quantities of interest, we are interested to compute the first statistical moment; that is, we only compute

$$\mathbb{E}\left[u_1^h\right](\mathbf{x}, t) = \int_{\mathcal{Y}} u_1^h(\mathbf{y}, \mathbf{x}, t) \rho(\mathbf{y}) \, d\mathbf{y} \tag{27}$$

and

$$\mathbb{E}\left[c_2^h\right](t) = \int_{\mathcal{Y}} c_2^h(\mathbf{y}, t) \rho(\mathbf{y}) \, d\mathbf{y}. \tag{28}$$

While all quantities of interest and their statistical moments are here given as time-dependent values, we will in practice always evaluate them for the final time $t = T$ of a given Navier–Stokes simulation only. This gives us a space-discrete function, cf. Eqs. (27), or a single number, cf. Eq. (28).

3.2 Stochastic Collocation

To underline the generality of the kernel-based stochastic collocation, we will consider a general quantity of interest $u : \mathcal{Y} \times \bar{\mathcal{D}} \times [0, T] \to \mathbb{R}$ for the rest of this section. We leave it to the reader to associate its approximation with the concrete examples of u_1^h and c_2^h, which were discussed before.

Following [6], stochastic collocation evaluates the quantities of interest with respect to $\mathbf{y}$ in collocation points,

$$Y_N := \{\mathbf{y}_1, \ldots, \mathbf{y}_N\} \subset \mathcal{Y}. \tag{29}$$

The point evaluations $u(\mathbf{y}_i, \mathbf{x}, t)$ are used to numerically approximate the continuous function,

$$u(\mathbf{y}, \mathbf{x}, t) \approx \sum_{i=1}^{N} u(\mathbf{y}_i, \mathbf{x}, t) L_i(\mathbf{y}) \quad \text{for all } \mathbf{y} \in \mathcal{Y}. \tag{30}$$

This is done with a Lagrange basis in a certain function (approximation) space $\mathcal{H}$ with respect to $\mathcal{Y}$, where the space $\mathcal{H}$ still needs to be specified; i.e.,

$$\{L_i\}_{i=1}^{N}, \quad L_i \in \mathcal{H}, \quad L_i : \mathcal{Y} \to \mathbb{R}, \quad \text{with } L_i(\mathbf{y}_j) = \begin{cases} 1 & i = j, \\ 0 & i \neq j. \end{cases} \tag{31}$$

Since each evaluation of the quantities of interest for a fixed parameter value $\mathbf{y} \in Y_N$ involves, e.g., a whole deterministic fluid dynamics simulation, we do not want the set Y_N to be of any regular gridlike structure. Grid like structures suffer in particular in a mesh refinement step. Typically, not just one point can be added at a time but several points have to be added in order to maintain the grid structure. Instead, we aim for a mesh-free collocation procedure.

Another issue is that we do not know the smoothness of the dependence of the quantities of interest on the parameters. This makes the use of approximation by reproducing kernels and in particular radial basis functions favorable since these methods are known to adapt to the smoothness of the function which is reconstructed once the radial basis function is chosen smooth enough and the point set Y_N is not too far from quasi-uniformity; see [22]. Consequently, we will choose the function space $\mathcal{H}$ to be a reproducing kernel Hilbert space (RKHS).

3.3 Reproducing Kernel Hilbert Spaces and Native Spaces

Following [23], a reproducing kernel Hilbert space is defined as a Hilbert space of functions,

$$\mathcal{H}_k(\mathcal{Y}) \subseteq \left\{ f : \mathcal{Y} \to \mathbb{R} \,\middle|\, \emptyset \neq \mathcal{Y} \subseteq \mathbb{R}^D \right\}, \tag{32}$$

which possesses a kernel function $k : \mathcal{Y} \times \mathcal{Y} \to \mathbb{R}$ that satisfies

$$k(\cdot, \mathbf{y}) \in \mathcal{H}_k(\mathcal{Y}) \quad \text{for all } \mathbf{y} \in \mathcal{Y} \quad \text{and} \tag{33}$$

$$f(\mathbf{y}) = (f, k(\cdot, \mathbf{y}))_{\mathcal{H}_k(\mathcal{Y})} \quad \text{for all } f \in \mathcal{H}_k(\mathcal{Y}) \text{ and all } \mathbf{y} \in \mathcal{Y}. \tag{34}$$

This kernel k is called the reproducing kernel. For two functions $f, g \in \mathcal{H}_k$ with $f = \sum_{j=1}^{N} \alpha_j^{(f)} k(\cdot, \mathbf{y}_j)$ the inner product is defined as $(f, g)_{\mathcal{H}_k} := \sum_{j=1}^{N} \sum_{j'=1}^{N} \alpha_j^{(f)} \alpha_{j'}^{(g)} k(\mathbf{y}_j, \mathbf{y}_{j'})$. A kernel k is called strictly positive definite on $\mathcal{Y} \subseteq \mathbb{R}^D$ if for all $N \in \mathbb{N}$, all pairwise distinct $Y_N = \{\mathbf{y}_1, \ldots, \mathbf{y}_N\} \subseteq \mathcal{Y}$, and all $\alpha \in \mathbb{R}^N \setminus \{0\}$ we have

$$\sum_{j=1}^{N} \sum_{k=1}^{N} \alpha_j \alpha_k \, k(\mathbf{y}_j, \mathbf{y}_k) > 0. \tag{35}$$

Note that it is possible to construct a RKHS $\mathcal{H}_k$ from a given strictly positive definite kernel function k. We then call $\mathcal{H}_k$ the native space of k; see [23].

3.4 Best Approximation and Regression in RKHS

Now, let a strictly positive definite kernel function k with its associated native space $\mathcal{H}_k(\mathcal{Y})$ be given. For the finite set of collocation points Y_N as in Eq. (29) we evaluate the kernel function k in these points. Thereby we introduce a finite-dimensional subspace,

$$\mathcal{H}_{Y_N} := \text{span}\{k(\cdot, \mathbf{y}_i) | \mathbf{y}_i \in Y_N\} \subset \mathcal{H} = \mathcal{H}_k, \tag{36}$$

of the reproducing kernel Hilbert space. Our aim is to approximate a given function $f \in \mathcal{H}_k$ by a function in $\mathcal{H}_{Y_N}$, i.e.,

$$f(\mathbf{y}) \approx \sum_{i=1}^{N} \alpha_i k(\mathbf{y}, \mathbf{y}_i). \tag{37}$$

It is well known that, if we only consider evaluations of f in the collocation points Y_N, we get the best approximation of f with respect to the native space norm by computing coefficients $\alpha := (\alpha_1, \dots, \alpha_N)^\top$ with

$$A_{k,Y_N} \alpha = \mathbf{f}, \tag{38}$$

where $\mathbf{f}$ is the data vector $(f(\mathbf{y}_1), \dots, f(\mathbf{y}_N))^\top$. Here, the matrix A_{k,Y_N} is given by

$$A_{k,Y_N} := \begin{pmatrix} k(\mathbf{y}_1, \mathbf{y}_1) & \dots & k(\mathbf{y}_1, \mathbf{y}_N) \\ \vdots & \ddots & \vdots \\ k(\mathbf{y}_N, \mathbf{y}_1) & \dots & k(\mathbf{y}_N, \mathbf{y}_N) \end{pmatrix}, \tag{39}$$

where the strict positive definiteness of k ensures invertibility of this system. We can build the Lagrange basis of $\mathcal{H}_{Y_N}$ by setting

$$(L_1(\mathbf{z}), \dots, L_N(\mathbf{z}))^\top := A_{k,Y_N}^{-1} (k(\mathbf{z}, \mathbf{y}_1), \dots, k(\mathbf{z}, \mathbf{y}_N))^\top. \tag{40}$$

This leads to an approximation of f in terms of the Lagrange basis of the form

$$f(\mathbf{y}) \approx \sum_{j=1}^{N} L_j(\mathbf{y}) f(\mathbf{y}_j). \tag{41}$$

Once the Lagrange basis is determined, this is a favorable way to represent interpolation.

From a practical point of view, the matrix A_{k,Y_N} may in general become ill-conditioned, depending on the kernel and the choice and number of collocation points. One approach to tackle this issue is the introduction of a regularization. A standard technique is the Tikhonov regularization [29]. It involves replacing the original linear system by

$$(A_{k,Y_N} + \epsilon_{reg} I_N)\alpha = \mathbf{f}, \tag{42}$$

with I_N the identity matrix. This regularization reduces the condition number of A_{k,Y_N}, but introduces a new error of the order of the regularization parameter ϵ_{reg}. Moreover, this regularization also accounts for the fact that we never deal with the true quantities of interest, e.g., $f = u$, but always with some numerical approximations of them. Hence, the regularized regression approach is favorable compared to classical interpolation. Nevertheless, we assume the data to be almost precise and hence ϵ_{reg} will be chosen very small, for example, $\epsilon_{reg} = 10^{-12}$ as in Section 4.1.

An alternative to Tikhonov regularization is regularization by a truncated singular value decomposition (TSVD) [30]. In this approach, a singular value decomposition of matrix A_{k,Y_N} is computed. The SVD is truncated for singular values below a given magnitude. Then, instead of solving the linear system $A_{k,Y_N} \alpha = \mathbf{f}$, the pseudo-inverse of the truncated matrix A_{k,Y_N} is applied to $\mathbf{f}$. In Section 4.2, we briefly compare numerical results with Tikhonov and TSVD regularization for a model problem.

3.5 Estimation of Stochastic Moments

The approximation of the stochastic moment $\mathbb{E}[u]$ needs the evaluation of an integral. To this end, conventional numerical quadrature methods like MC, QMC, or sparse grids, etc. could be employed. Here, we restrict ourselves to kernel-based interpolatory quadrature rules. We have

$$\mathbb{E}[u](\mathbf{x}, t) = \int_{\mathcal{Y}} u(\mathbf{y}, \mathbf{x}, t)\rho(\mathbf{y}) \, d\mathbf{y} \approx \sum_{i=1}^{N} u(\mathbf{y}_i, \mathbf{x}, t) \int_{\mathcal{Y}} L_i(\mathbf{y})\rho(\mathbf{y}) d\mathbf{y}, \tag{43}$$

with the Lagrange basis from Eq. (40). Moreover, we can reduce the integral,

$$\int_{\mathcal{Y}} L_i(\mathbf{y})\rho(\mathbf{y})d\mathbf{y} = \sum_{j=1}^{N} c_{i,j}^h \int_{\mathcal{Y}} k(\mathbf{y},\mathbf{y}_j)\rho(\mathbf{y})d\mathbf{y}, \tag{44}$$

to linear combinations of integrals over the kernel where the coefficients are given as $A_{k,Y_N}^{-1} = (c_{i,j}^h)_{1\le i,j\le N}$. In order to approximate the kernel integral in Eq. (44), we employ here for the reason of simplicity full tensor-product Clenshaw-Curtis quadrature but also any other suitable method will do. Hence, the quadrature points are in general different from the sampling points. Note here that the quadrature of the kernel functions can be made arbitrarily precise and once the collocation points are designed, the integral in Eq. (44) can be precomputed anyway. Moreover, we do not consider the numerical costs for the quadrature. This is due to the fact that a sampling point corresponds to a full three-dimensional two-phase fluid simulation and hence is much more costly than a quadrature point.

3.6 Sampling in $\mathcal{Y}$ and Choice of Kernels

As collocation points Y_N, we use low discrepancy point sets. They have the advantage that they allow one to produce almost quasi-uniform point sets in higher dimensions. Since kernel-based methods can work on arbitrarily scattered point sets, the specific choice is not crucial for the remainder of this article. We use so-called *quasi-random* sequences $Z_{QMC} := \{\mathbf{z}_i\}_{i=1}^N$ to sample collocation points. Quasi-random sequences are designed to have a small discrepancy [31]. Here, to be precise, we employ multidimensional Halton sequences. The ith element of a D-dimensional Halton sequence in $[0,1)^D$ is given as

$$\mathbf{z}_i = (\psi_{R_1}(i), \psi_{R_2}(i), \ldots, \psi_{R_D}(i))^\top, \tag{45}$$

$$\psi_R(i) = \sum_{j=1}^{\infty} a_j(i)R^{-j}, \quad \text{with} \quad i = \sum_{j=1}^{\infty} a_j(i)R^{j-1}. \tag{46}$$

Here, the sums are all finite and the R_k have to be coprime integers, and the $a_j(i)$ just denote the R-adic representation of i. We employ the Halton points here, since we work in moderately high dimensions. We are well aware of the fact that Halton points might deteriorate in high dimensions and scrambling might be needed then; see [32–34]. Moreover, we stress that we work with a kernel-based and hence mesh-free method. This implies that our methods work on all scattered point sets and only the theoretical convergence analysis is affected by the distribution properties of the point set.

Our approach was so far described for any suitable RKHS. The final question is now what types of RKHS we want to invoke and what the associated kernel $k : \mathcal{Y} \times \mathcal{Y} \to \mathbb{R}$ will be. To this end, we restrict ourselves to radial basis functions/radial kernels. They are given by

$$k(\mathbf{y},\mathbf{y}') := \varphi(\|\mathbf{y}-\mathbf{y}'\|_2), \tag{47}$$

with an appropriate function $\varphi : \mathbb{R}^{\ge 0} \to \mathbb{R}$.

There are several examples of such radial kernels. Table 1 summarizes the kernel functions used in this work and the Sobolev spaces that are equal to their native space.

Wendland kernels $k_{d,k}$ [23] are compactly supported functions with some minimality properties for the degrees of the polynomials involved in their construction. They are positive definite and it holds that $\varphi_{D,k} \in C^{2k}(\mathbb{R})$. For their associated $k_{D,k}$ for $k=0,1$ we, e.g., have

$$\varphi_{D,0}(r) = (1-r)_+^{\lfloor D/2 \rfloor+1}, \quad \varphi_{D,1}(r) = (1-r)_+^{\ell+1}[(\ell+1)r+1], \tag{48}$$

with $\ell := \lfloor D/2 \rfloor + k + 1$ and the notation $(r)_+ = \begin{cases} r & \text{if} \quad r \ge 0, \\ 0 & \text{if} \quad r < 0. \end{cases}$

The Matérn kernels k_β with $\beta > d/2$ use in their definition K_ν and $\mathcal{Y}$, which are the modified Bessel function of the second kind of order ν and the Gamma function; see also [23]. These kernels are strictly positive definite as

TABLE 1: The above radial kernel functions are used in this work to build native (approximation) spaces. The resulting native spaces are well-known Sobolev spaces

Kernel	Definition	Sobolev space
Wendland	$k_{D,k}(\mathbf{y}, \mathbf{y}') := \varphi_{D,k}(\|\mathbf{y} - \mathbf{y}'\|)$	$H^{D/2+k+1/2}(\mathbb{R}^D)$
Matérn	$k_\beta(\mathbf{y}, \mathbf{y}') := (K_{\beta-D/2}(\|\mathbf{y} - \mathbf{y}'\|)\|\mathbf{y} - \mathbf{y}'\|^{\beta-D/2})/2^{\beta-1}\mathcal{Y}(\beta)$	$W^{\beta,2}(\mathbb{R}^D)$
Gaussian	$k_\epsilon(\mathbf{y}, \mathbf{y}') := \varphi_\epsilon(\|\mathbf{y} - \mathbf{y}'\|) := e^{-\epsilon^2\|\mathbf{y}-\mathbf{y}'\|^2}$	n/a

long as $d < 2\beta$. According to [35, Section 4.4], we have for special choices of parameter β simplified representations of the Matérn kernel function (up to a dimension-dependent scaling constant), e.g.,

$$k_{(D+1)/2}(\mathbf{y}, \mathbf{y}') := e^{-\|\mathbf{y}-\mathbf{y}'\|}, \quad k_{(D+3)/2}(\mathbf{y}, \mathbf{y}') := (1 + \|\mathbf{y} - \mathbf{y}'\|)e^{-\|\mathbf{y}-\mathbf{y}'\|}. \tag{49}$$

The last example is the well-known Gaussian kernel with $\epsilon \in \mathbb{R}^+$ as the scaling parameter. It is special in the sense that its native space is contained in every Sobolev space.

4. NUMERICAL RESULTS

In the following, we will discuss our method for two analytic test cases and several two-phase flow problems. After the introduction of the setup, empirical convergence results will be presented for kernel-based stochastic collocation using different kernel functions. At the end of this section, we also briefly compare results from our kernel-based approach with a sparse grid approach for stochastic collocation.

4.1 Setup

In this section, we first consider the approximation of means of two analytic test functions; cf. Section 4.2. Thereafter, we compute approximations to the field $\mathbb{E}[u_1^h](\mathbf{x}, T)$ and the scalar $\mathbb{E}[c_2^h](T)$ for fixed T. The deterministic evaluations of the quantities of interest u_1^h and c_2^h are done using NaSt3DGPF for each $\mathbf{y}_i \in \mathcal{Y}$. Since this solver uses a finite volume/finite difference method on a staggered grid, we obtain scalar-valued, space-dependent fields as grid functions on a regular grid with $M^h := M$ points. Here, the parameter h, which will be dismissed in the remainder, indicates that the M points correspond to a grid in space with uniform mesh size h and an accordingly chosen CFL conforming time step. In case of the quantity of interest u_1^h, we thus actually compute pointwise for every grid point the first moment $\mathbb{E}[u_1^h](T) \in \mathbb{R}^M$. The quantity $\mathbb{E}[c_2^h](T)$ is a single number.

To approximate these quantities with respect to the stochastic space, we use the RBF kernel-based stochastic collocation method. If not stated otherwise, the applied kernel functions are the Gaussian kernel k_ϵ with scaling parameter $\epsilon = 1.0$, compactly supported Wendland kernels $k_{D,k}$ with smoothness parameters $k = 0, 1, 2, 3$, and appropriate dimensionality D and the Matérn kernel k_β with parameter $\beta = (D + 3)/2$. Remember that we call the dimension of the stochastic space D; thus $\mathcal{Y} \subset \mathbb{R}^D$. The regularization parameter, cf. Section 3.4, is set to $\epsilon_{reg} = 10^{-12}$. The kernel interpolation problem is solved by direct LU factorization. Radial basis functions are isotropic, by standard; thus the norm involved in their construction is the (scaled) Euclidean distance $\|\cdot\| := \zeta\|\cdot\|_2$, with a default of $\zeta = 1.0$. In Section 4.2, we briefly compare different choices of ζ for a model problem. The N collocation points are generated from a Halton sequence of appropriate dimension.

Quadrature is carried out by a full tensor-product rule constructed by univariate Clenshaw-Curtis quadrature rules with $2^{l_q-1} + 1$ nodes, if not indicated differently. The quadrature level is usually $l_q = 7$. Sparse grid quadrature rules are used whenever the dimensionality of the stochastic space would lead to prohibitive computational run times and memory requirements.

In the empirical convergence studies, the reference solutions will be computed on an extremely fine grid. We will use a subscript H to denote the reference solutions. Moreover, in order to visualize the numerical error, we approximatively compute the expectation of the reference solution as

$$\mathbb{E}\big[u_i^H\big](\mathbf{x}, T) := \int_{\mathcal{Y}} u_i^H(\mathbf{y}, \mathbf{x}, T)\rho(\mathbf{y})d\mathbf{y} \approx \sum_{n=1}^{N_{\max}} u_i^H(\tilde{\mathbf{y}}_n, \cdot, T) \int_{\mathcal{Y}} \tilde{L}_n(\mathbf{y})\rho(\mathbf{y})d\mathbf{y}, \tag{50}$$

where $\tilde{Y}_{N_{\max}} \subset \mathcal{Y}$ denotes a fine sampling set, i.e., $N_{\max} \gg N$. Here, $\tilde{L}$ is computed based on a possibly different kernel compared to the approximation.

4.2 Problems with Analytic Solution

Before we discuss numerical results for the challenging two-phase Navier–Stokes application problem, we briefly analyse the properties of the kernel-based stochastic collocation for two representative test cases with analytic solution. To this end, we restrict ourselves to a simple model problem.

The first test case is an elliptic PDE with random coefficient similar to [36]. The parameter space is $(\mathcal{Y}, \mathcal{B}, \rho\, d\mathbf{y})$ with $\mathcal{Y} \subset \mathbb{R}$ and stems from a one-term Karhunen–Loève expansion of a random coefficient. We want to approximate $\mathbb{E}[u]$ with $u : \mathcal{Y} \times [-0.5, 0.5]^2 \to \mathbb{R}$ being the solution of

$$-\nabla \cdot (a(\mathbf{y}, \mathbf{x})\nabla u(\mathbf{y}, \mathbf{x})) = f(\mathbf{x}) \qquad \text{in } \mathcal{Y} \times (-0.5, 0.5)^2, \tag{51}$$

$$u(\mathbf{y}, \mathbf{x}) = 0 \qquad \text{on } \mathcal{Y} \times \partial(-0.5, 0.5)^2, \tag{52}$$

with the random diffusion coefficient $a(\mathbf{y}, \mathbf{x}) = 1 + \sigma(1/\pi^2)y_1 \cos\big((\pi/2)\big(x_1^2 + x_2^2\big)\big)$; thus we have $\mathbf{y} = y_1$. The right-hand side term is given as

$$f(\mathbf{y}, \mathbf{x}) = 32\left(1 + \sigma + \frac{y_1 \cos((1/2)\pi(x_1^2 + x_2^2))}{\pi^2}\right)e^{-y_1^2}\left(x_2^2 - \frac{1}{2} + x_1^2\right)$$
$$- \frac{32}{\pi}y \sin\left(\frac{1}{2}\pi(x_1^2 + x_2^2)\right)\left(x_1^2 e^{-y_1^2}\left(x_2^2 - \frac{1}{4}\right) + x_2^2 e^{-y_1^2}\left(x_1^2 - \frac{1}{4}\right)\right).$$

With this construction, it is possible to derive an exact solution of the parametric PDE problem as

$$u(\mathbf{y}, \mathbf{x}) = 16\, e^{-y_1^2}\left(x_1^2 - \frac{1}{4}\right)\left(x_2^2 - \frac{1}{4}\right). \tag{53}$$

The variable y_1 corresponds to the random variable $Y_1(\omega) \sim \mathcal{U}(-\sqrt{3}, \sqrt{3})$; thus we employ the density function $\rho(\mathbf{y}) = 1/2\sqrt{3}$. It is possible to derive the exact mean as $\mathbb{E}[u] = (1/6)\,\mathrm{erf}\big(\sqrt{3}\big)\sqrt{3}\sqrt{\pi}\big(16x_1^2 x_2^2 - 4x_1^2 - 4x_2^2 + 1\big)$.

The convergence study for the mean is presented on the left-hand side of Fig. 2. It shows absolute errors of the mean solution field with respect to the exact solution measured in a discrete l_2 norm and compares different kernel choices. The regularization parameter ϵ_{reg} is set to 10^{-15} for the Gaussian kernel. All other parameters remain at the previously defined values; see Section 4.1. Approximation with the Gaussian kernel leads to an almost perfect solution, i.e., machine precision with only two collocation points, which is due to the specific choice of the unknown function u. All other kernels give algebraic convergence rates with measured approximate orders 2, 3, 4, and 5 for Wendland kernels with $k = 0, 1, 2, 3$, and third-order convergence for that specific choice of a Matérn kernel. Convergence saturates between machine accuracy and the size of the regularization parameter, which, in contrast to the Gaussians, is set to $\epsilon_{reg} = 10^{-12}$ for these kernels.

On the right-hand side of Fig. 2, we repeat the same convergence study. However, we now fix the Wendland kernel $k_{1,3}$ and change the scaling ζ. The results indicate that this scaling has a substantial influence on the convergence of the method. In the given results, a choice of ζ, which is too large, leads to a longer preasymptotic regime. A choice of ζ, which is too small, leads to convergence issues. For the rest of this paper, we will manually optimize this parameter.

Figure 3 shows results for the use of Tikhonov regularization on the left-hand side and for the use of the truncated SVD on the right-hand side. As before, we approximate the mean, fixing the kernel function $k_{1,3}$. However, we do variations in either the regularization parameter ϵ_{reg} (for Tikhonov) or in the dropping tolerance for singular values (for TSVD). Both approaches show similar regularization properties, i.e., stronger regularization leads to a higher
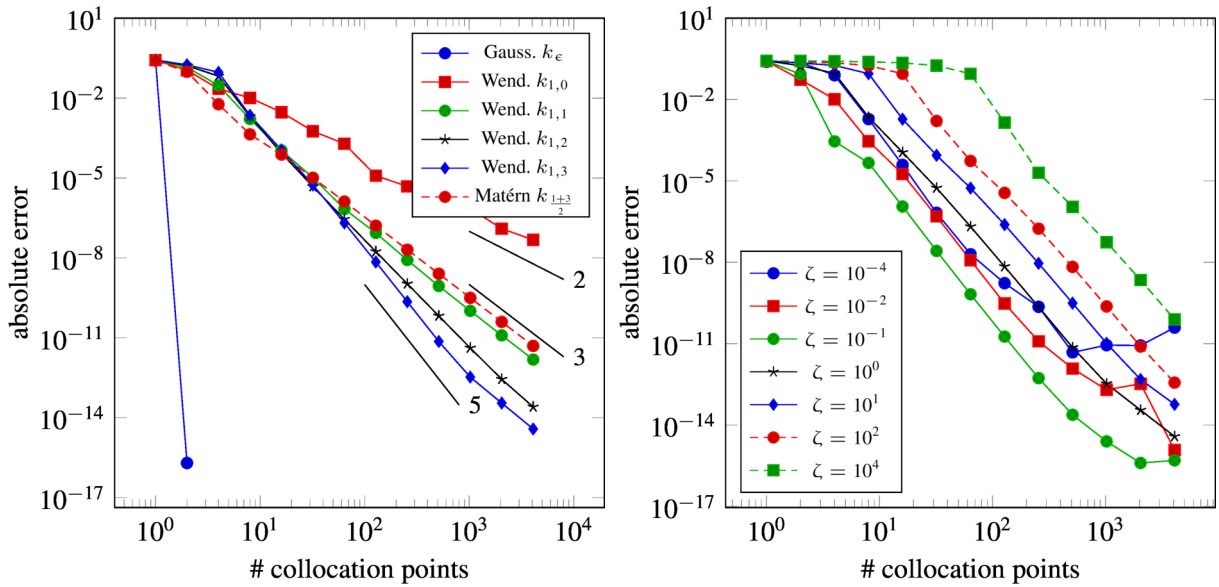
FIG. 2: Error convergence analysis for the mean approximation in the random-coefficient Poisson problem test case Eqs. (51) and (52) with $D = 1$. Left: Comparison of different kernel functions. Right: Comparison of different scalings ζ for the fixed kernel function $k_{1,3}$.
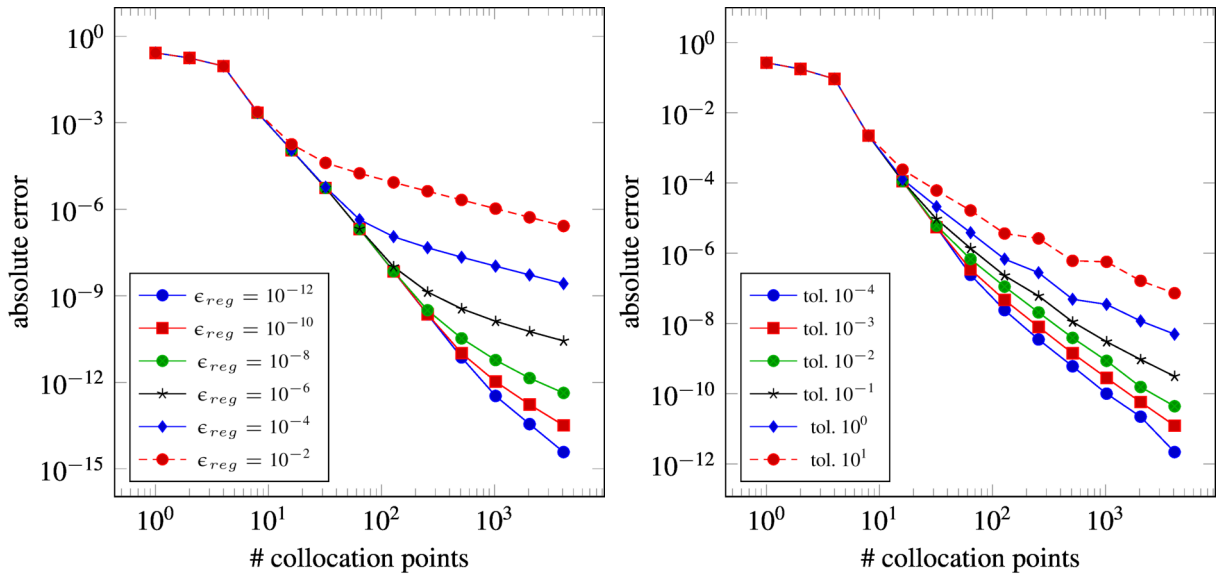

FIG. 3: Comparison of the Tikhonov regularization (left) and the TSVD regularization (right) for the random-coefficient Poisson problem test case. The same Wendland kernel is applied.

total error in the approximation. Throughout the rest of this work, we will use Tikhonov regularization, since this approach seemed to be numerically more stable for smaller regularization.

As a higher-dimensional test problem with limited smoothness, we further consider the function

$$u(\mathbf{y}) = \prod_{m=1}^{D} \frac{|4y_m - 2| + a_m}{1 + a_m}; \tag{54}$$

cf. [37]. Here, we approximate the exact mean $\mathbb{E}[u] = 1$ with the choices $a_m = (m-2)/2$, $\rho(\mathbf{y}) = 1$. Moreover, the y_m are realizations of independent random variables $Y_m(\omega) \sim \mathcal{U}(0,1)$.

In the numerical results, the scaling of the Gaussian kernel is set to $\epsilon = 2.0$. Furthermore the approximation by the Gaussian kernel is regularized with a regularization parameter $\epsilon_{reg} = 10^{-8}$. We set $D = 3$. Figure 4 shows the error behavior of the mean of this model problem for different kernels. We observe convergence rates which are better than that for Monte Carlo and even better than that for quasi Monte Carlo methods. However, all kernel functions show qualitatively identical results. This suggests that all results are affected by the limited smoothness of the function (54), in the first place.

4.3 Bubble Flow under Random Volume Force

Our first application for the two-phase Navier–Stokes equations is a rising air bubble in water under a random volume force field with known covariance spectrum. The random force field is approximated by a truncated Karhunen–Loève expansion. All other parameters are deterministic. Figure 5 outlines the basic setup of the two-phase flow problem[‡]. The domain is given as $\bar{\mathcal{D}} = [0, 0.2]^3$ and the fluid flow is computed up to $T = 0.35$ sec. Since an air-water system shall be analyzed, we have the densities $\rho_1 = 1000$ and $\rho_2 = 1$ and viscosities $\mu_1 = 1.002 \times 10^{-3}$ and $\mu_2 = 1.72 \times 10^{-5}$.[§] The initial conditions are set to $\mathbf{u}_{0_i}^h = (0,0,0)^\top$. Moreover, the surface tension coefficient is set to $\sigma = 0.0728$ which reflects the parameter of a water-air interface. Boundary conditions of the velocity field are described in terms of a boundary operator,

$$\mathcal{B}\mathbf{u}^h := \left(\mathbf{u}^h \cdot \mathbf{n}_\Gamma^h, \frac{\partial(\mathbf{u}^h \cdot \mathbf{s}_\Gamma^h)}{\partial \mathbf{n}_\Gamma^h}, \frac{\partial(\mathbf{u}^h \cdot \mathbf{t}_\Gamma^h)}{\partial \mathbf{n}_\Gamma^h} \right)^\top = (0,0,0)^\top = b_\Gamma, \tag{55}$$
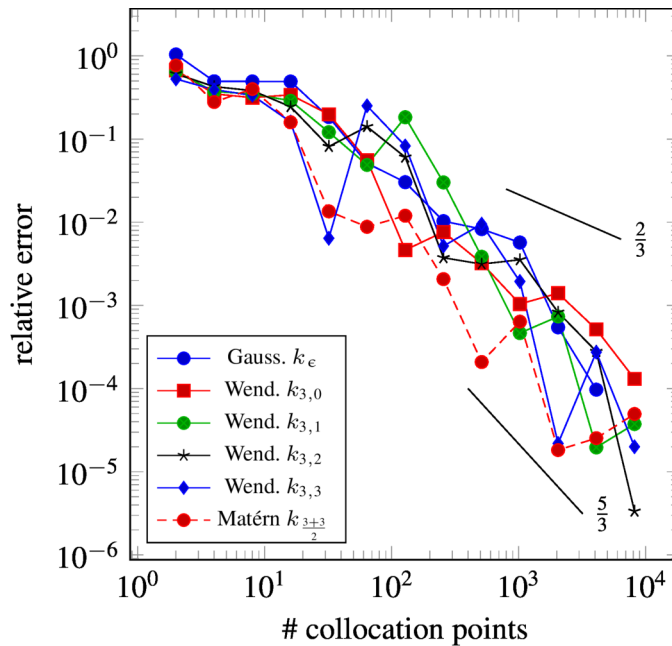

FIG. 4: Error convergence analysis for the mean approximation comparing different kernel functions for the function (54)

[‡] Note that some quantities have physical units. We do not write them every time in order to keep the notation simple. We will assume the densities ρ in $[\text{kg} \cdot \text{m}^{-3}]$, the viscosities in $[\text{kg} \cdot \text{m}^{-1} \cdot \text{s}^{-1}]$, the surface tension in $[\text{N} \cdot \text{m}^{-1}]$, and the gravitational force $\mathbf{g}$ in $[\text{ms}^{-2}]$.
[§] The dimensionless Reynolds number is given as $\text{Re} = \rho v L/\mu$, where v and L are the characteristic velocity and the characteristic length. Here, the Reynolds number is in the range $\text{Re} \in [10^4, 10^6]$. The validity of the discretization in the regime presented here was shown in [10].
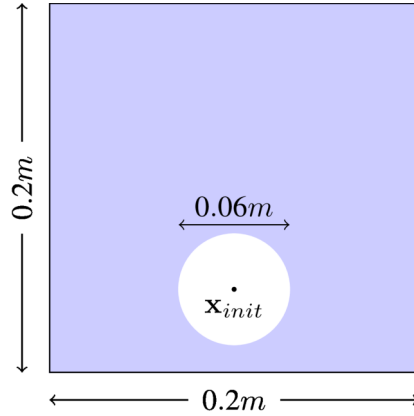
FIG. 5: Two-dimensional side view of the three-dimensional rising bubble application setup

with the notation as in Eq. (4). Thus, infinite slip is assumed on the boundary. Furthermore, the initial position of the center of the bubble is $\mathbf{x}^{init} = (0.1, 0.06, 0.1)^{\top}$. The phasewise subdomains $\mathcal{D}_1^h, \mathcal{D}_2^h$ are given by

$$\mathcal{D}_i^h(t) = \Phi\big[(\mathcal{D}_i^h)^0\big](t). \tag{56}$$

Here, Φ describes the transformation of the initial domains $(\mathcal{D}_i^h)^0 := \mathcal{D}_i^h(t = 0)$ under fluid flow. These initial domains are defined such that the gas phase is a sphere of radius 0.03 m; thus

$$(\mathcal{D}_1^h)^0 := \{\mathbf{x} \in \mathcal{D} | \|\mathbf{x} - \mathbf{x}_{init}\| > 0.03\}, \tag{57}$$

$$(\mathcal{D}_2^h)^0 := \{\mathbf{x} \in \mathcal{D} | \|\mathbf{x} - \mathbf{x}_{init}\| < 0.03\}. \tag{58}$$

The initial free surface is $\Gamma_f(t = 0) = \mathcal{D} \setminus (\mathcal{D}_1^0 \cup \mathcal{D}_2^0)$. In order to model a stochastic/parametric volume force g, we consider a lognormal random field g_{L_c} with $\mathbb{E}[g_{L_c}] \equiv -9.81$ and

$$\text{Cov}[\log(g_{L_c} - (-9.81))](x, x') = e^{-(x-x')^2/L_c^2}, \tag{59}$$

where the correlation length is assumed to be $L_c = 2.0$. The random field g_{L_c} is approximated by a truncated Karhunen–Loève expansion resulting in g_{D,L_c}. Consequently,

$$\log(g_{L_c}(\mathbf{y}, \mathbf{x}) + 9.81) \approx \log(g_{D,L_c}(\mathbf{y}, \mathbf{x}) + 9.81) := 1 + y_1 \left(\frac{\sqrt{\pi}L_c}{2}\right)^{1/2} + \sum_{m=2}^{D} \lambda_m \phi_m(x_2) y_m, \tag{60}$$

with truncation after D expansion terms. Here, the $\{y_m\}_{m=1}^D$ correspond to the independent random variables $\{Y_m(\omega)\}_{m=1}^D$ with each $Y_m \sim \mathcal{U}(-\sqrt{3}, \sqrt{3})$; thus $\rho(\mathbf{y}) = \left(1/2\sqrt{3}\right)^D$. Furthermore, the eigenvalues and eigenfunctions are given as

$$\lambda_m := (\sqrt{\pi}L_c)^{1/2} \exp\left(\frac{-(\lfloor m/2 \rfloor \pi L_c)^2}{8}\right), \quad \phi_m(x_2) := \begin{cases} \sin(\lfloor m/2 \rfloor \pi x_2) & \text{if } m \text{ even,} \\ \cos(\lfloor m/2 \rfloor \pi x_2) & \text{if } m \text{ odd,} \end{cases} \tag{61}$$

with $m > 1$. Finally, the volume force is set to

$$\mathbf{g}(\mathbf{y}, \mathbf{x}) := (0, g_{D,L_c}(\mathbf{y}, x_2), 0)^{\top}. \tag{62}$$

This two-phase flow problem is now discretized in space by a mesh of $M = 100^3$ grid points. Time discretization is done with a second-order Adams–Bashforth method and adaptive time-step size control. The Karhunen–Loève

expansion is truncated after $D = 3$ terms (mainly for performance reasons). The correlation length is set to $L_c = 2.0$. The norm in the radial basis function construction is $\| \cdot \| := \zeta \| \cdot \|_2$, with $\zeta = 0.1$ for the Gaussian kernel and all Wendland kernels and $\zeta = 1.0$ for the Matérn kernel. The reference moment as in Eq. (50) is computed by a Gaussian kernel with $N_{\text{max}} = 1024$ collocation points. Quadrature follows the default of tensor-product quadrature with an approximation level of $l_q = 7$.

Figure 6 displays visualizations of four solution realizations at $T = 0.2$ sec. The bubble is shown by extracting the isosurface of the zero level-set function. Furthermore, a slice of the velocity field with coloring by the magnitude and velocity field streamlines is given.

On the left-hand side in Fig. 7, a visualization of the mean velocity field $\mathbb{E}[\mathbf{u}^h]$ by means of a slice of streamlines through all three mean velocity field components is shown. The diagram in Fig. 7(right) displays the convergence of the approximation of $\mathbb{E}[u_1^h](T)$ for different kernel functions with respect to the reference solution. We observe that rates in the range of 0.75 are achieved by the Wendland and Matérn kernels. There is a slight reduction of the convergence rate for smoother Wendland kernels. However, the convergence results obtained by the Gaussian kernel clearly show higher-order and maybe even an exponential convergence behavior might be anticipated here. This suggests a smooth dependence of the quantity of interest on the random input.
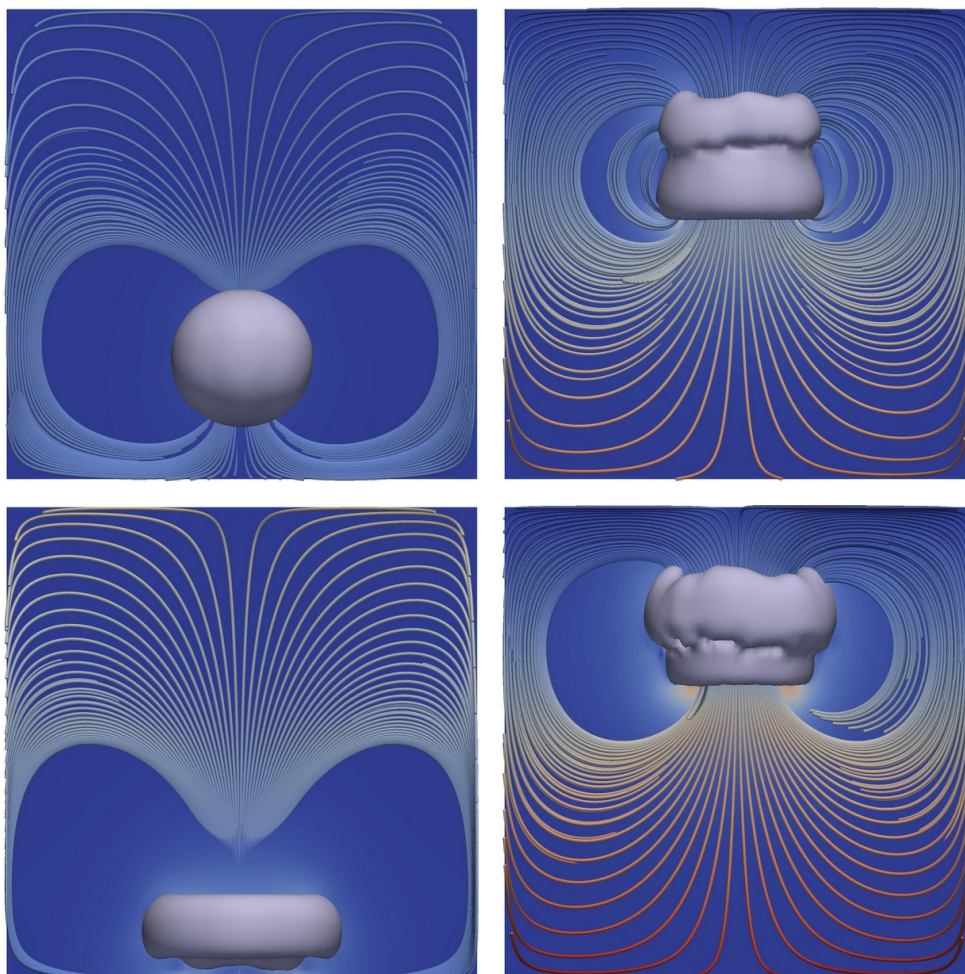

FIG. 6: Visualizations of flow field solutions of the bubble flow with random volume force and $D = 3$ at $T = 0.2$ seconds for stochastic parameters $\mathbf{y}_1 \approx (0.0, -0.58, -1.04)^\top$, $\mathbf{y}_{12} \approx (-1.08, -1.22, -0.07)^\top$, $\mathbf{y}_{19} \approx (0.97, -0.32, 1.45)^\top$, and $\mathbf{y}_{411} \approx (1.21, -0.93, -0.72)^\top$ (from left to right)
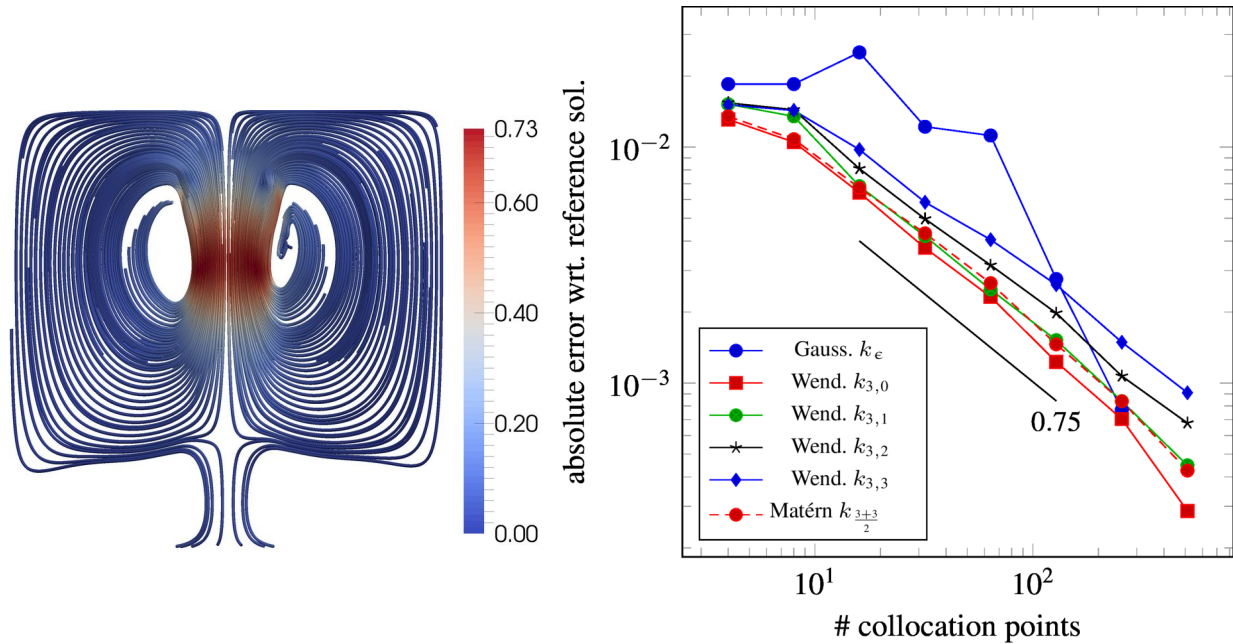
FIG. 7: Streamline slice visualization of the mean velocity field with color-coded velocity magnitude in the bubble flow problem with random volume forces (left) and error convergence results for the first component of the mean velocity field $\mathbb{E}[u_1^h](T)$ (right)

4.4 Rising Bubble Flow in a Random Situation

Our second application for the two-phase Navier-Stokes equations uses a similar setup as the first flow example. We again consider a rising air bubble in some liquid. Now, however, the density, viscosity, and initial bubble position are under stochastic influence, whereas the volume forces are deterministically given.

Again Fig. 5 outlines the basic setup of this two-phase flow problem. The domain is given as $\bar{\mathcal{D}} = [0, 0.2]^3$ and we have $T = 0.35$. The volume force $\mathbf{g}$ is given as standard gravity. The initial conditions are also set to $\mathbf{u}_{0_i} = (0, 0, 0)^\top$. Furthermore, the surface tension coefficient is $\sigma = 0.0728$. The boundary conditions are the same as in the previous test case. The gas phase $\mathcal{D}_2$ once more modeled as air; i.e., the density is $\rho_2 = 1$, and the viscosity is $\mu_2 = 1.72 \times 10^{-5}$. The remaining quantities are assumed to be random. The missing random density ρ_1 and viscosity μ_1 will be given in Eq. (67). The initial position of the air bubble shall be a random quantity; see Eq. (66). This means that the phasewise subdomains $\mathcal{D}_1^h, \mathcal{D}_2^h$ (or the level-set function describing them) are stochastic processes themselves. Therefore, these domains are given for time t by $\mathcal{D}_i^h(\mathbf{y}, t)$ with

$$\mathcal{D}_i^h(\mathbf{y}, t) = \Phi[(\mathcal{D}_i^h)^0(\mathbf{y})](t), \quad (\mathcal{D}_i^h)^0(\mathbf{y}) := \mathcal{D}_i^h(\mathbf{y}, 0), \quad y \in \mathcal{Y}, \tag{63}$$

where Φ again describes the transformation of the initial domains $(\mathcal{D}_i^h)^0(\mathbf{y})$ under fluid flow. It deterministically depends on the velocities u_1, u_2, but the initially given domains are subject to random perturbations. We define the initial liquid and gas phase domains $\mathcal{D}_1^0(\mathbf{y})$ and $(\mathcal{D}_2^h)^0(\mathbf{y})$ such that the gas phase domain is a sphere of radius $0.03\,m$ around some random initial center $\mathbf{x}_{init}(\mathbf{y})$ at the beginning, thus

$$(\mathcal{D}_1^h)^0(\mathbf{y}) := \{\mathbf{x} \in \mathcal{D} | \|\mathbf{x} - \mathbf{x}_{init}(\mathbf{y})\| > 0.03\}, \tag{64}$$

$$(\mathcal{D}_2^h)^0(\mathbf{y}) := \{\mathbf{x} \in \mathcal{D} | \|\mathbf{x} - \mathbf{x}_{init}(\mathbf{y})\| < 0.03\}. \tag{65}$$

The initial free surface is $\Gamma_f(\mathbf{y}, 0) = \mathcal{D}^h \setminus ((\mathcal{D}_1^h)^0(\mathbf{y}) \cup (\mathcal{D}_2^h)^0(\mathbf{y}))$. Moreover, the random parameter functions $x_1^{init}(\mathbf{y})$, $x_2^{init}(\mathbf{y})$, and $x_3^{init}(\mathbf{y})$ with $\mathbf{x}_{init}(\mathbf{y}) = (x_1^{init}, x_2^{init}, x_2^{init})$ as well as the material parameters for the liquid

phase, $\mu_1(\mathbf{y})$ and $\rho_1(\mathbf{y})$, are modeled by truncated Karhunen–Loève expansions. Truncation is done after the first stochastic term. Overall, these functions are given as

$$x_1^{init}(\mathbf{y}) = 0.1 + \frac{0.06}{\sqrt{3}} y_1^{x_1}, \quad x_2^{init}(\mathbf{y}) = 0.06 + \frac{0.01}{\sqrt{3}} y_1^{x_2}, \quad x_3^{init}(\mathbf{y}) = 0.1 + \frac{0.06}{\sqrt{3}} y_1^{x_3}, \tag{66}$$

$$\mu_1(\mathbf{y}) = 0.5005 + \frac{0.4995}{\sqrt{3}} y_1^{\mu_1}, \quad \rho_1(\mathbf{y}) = 750 + \frac{250}{\sqrt{3}} y_1^{\rho_1}. \tag{67}$$

All parameters of this problem are now collected in the five-dimensional vector $\mathbf{y}$ with $\mathbf{y} = (y_1^{x_1}, y_1^{x_2}, y_1^{x_3}, y_1^{\mu_1}, y_1^{\rho_1})^\top$. We assume $\mathbf{y}$ to be a realization of the independent random vector Y with

$$Y_1^{x_1} \sim \mathcal{U}\left(-\sqrt{3}, \sqrt{3}\right), \quad Y_1^{x_2} \sim \mathcal{U}\left(-\sqrt{3}, \sqrt{3}\right), \quad Y_1^{x_3} \sim \mathcal{U}\left(-\sqrt{3}, \sqrt{3}\right), \tag{68}$$

$$Y_1^{\mu_1} \sim \mathcal{U}\left(-\sqrt{3}, \sqrt{3}\right), \quad Y_1^{\rho_1} \sim \mathcal{U}\left(-\sqrt{3}, \sqrt{3}\right). \tag{69}$$

Consequently, the density function becomes $\rho(\mathbf{y}) = \left(1/2\sqrt{3}\right)^5$. Here, we again approximate the first stochastic moment $\mathbb{E}\left[u_1^h\right](T)$.

This flow problem is now discretized using a uniform grid with $M = 100^3$ grid points, a finite-difference discretization in space, and a second-order Adams–Bashforth method with adaptive time stepping in time. We apply the stochastic approximation in the image of the five random input variables (see also Eqs. (66) and (67)); thus a stochastic space $\mathcal{Y}' = [0.04, 0.16] \times [0.05, 0.07] \times [0.04, 0.16] \times [0.001, 0.1] \times [500, 1000]$ is considered. To approximate this space uniformly, the norm

$$\|\mathbf{y}'\| := \zeta \left\| \left(5x_1^{init}, 5x_2^{init}, 5x_3^{init}, \mu_1, 10^3 \rho_1\right) \right\|_2 \tag{70}$$

is used in the construction of the radial basis functions. Approximation by Gaussian kernels is done with $\zeta = 0.1$, while the other kernels have $\zeta = 1.0$. All other approximation parameters are set as mentioned in Section 4.1.

Figure 8 shows four flow field realizations at $T = 0.2\,s$. Approximation results for the mean of the velocity field at $T = 0.2\,s$ are given in Fig. 9 the left, a streamline slice visualization of the reference solution is shown, which is approximated by the Gaussian kernel with $N_{\max} = 512$ collocation points. On the right-hand side, error convergence in the mean $\mathbb{E}\left[u_1^h\right](T)$ of the first component of the velocity field is given for different kernel functions. We observe that rates in the range of 0.7–0.8 are achieved by Wendland, Matérn, and Gauss kernels. The use of higher-order Wendland kernels does not result in any improvement. The highest convergence rates are achieved by the Gaussian and the Matérn kernel with about 0.8.

4.5 Comparison to Sparse Spectral Tensor-Product Approximations

In this section, our proposed kernel-based stochastic collocation method is compared to sparse grid approximations. To this end, we employ on the one hand our kernel-based method with the default parameter chosen as in Section 4.1, and on the other hand the sparse grid method within the *Dakota* framework [38]. Dakota is a parallel software suite developed by the Sandia National Laboratories. It allows, one e.g., to apply optimization and uncertainty quantification for black-box solvers. Dakota features, among others, sparse grid stochastic collocation.

Classical stochastic collocation as provided by Dakota uses univariate Lagrange polynomials as Lagrange basis functions [6]. For multivariate interpolation, i.e., higher dimensions in stochastic space, a Smolyak sparse grid construction as in [6] is used. More details on the Dakota-based implementation of the Smolyak sparse grid construction are given in [38]. The employed parameters for sparse grid stochastic collocation in Dakota are depicted in Configuration 1 in Appendix A. We will employ the Dakota implementation for the numerical comparison in Fig. 10.

Note here that we do not consider *anisotropic* sparse grid constructions [39], because the RBF kernel-based stochastic collocation is employed without any directional preference anyway. However, the topic of dimension-wise weighting is future work and has been already partially considered in [21].
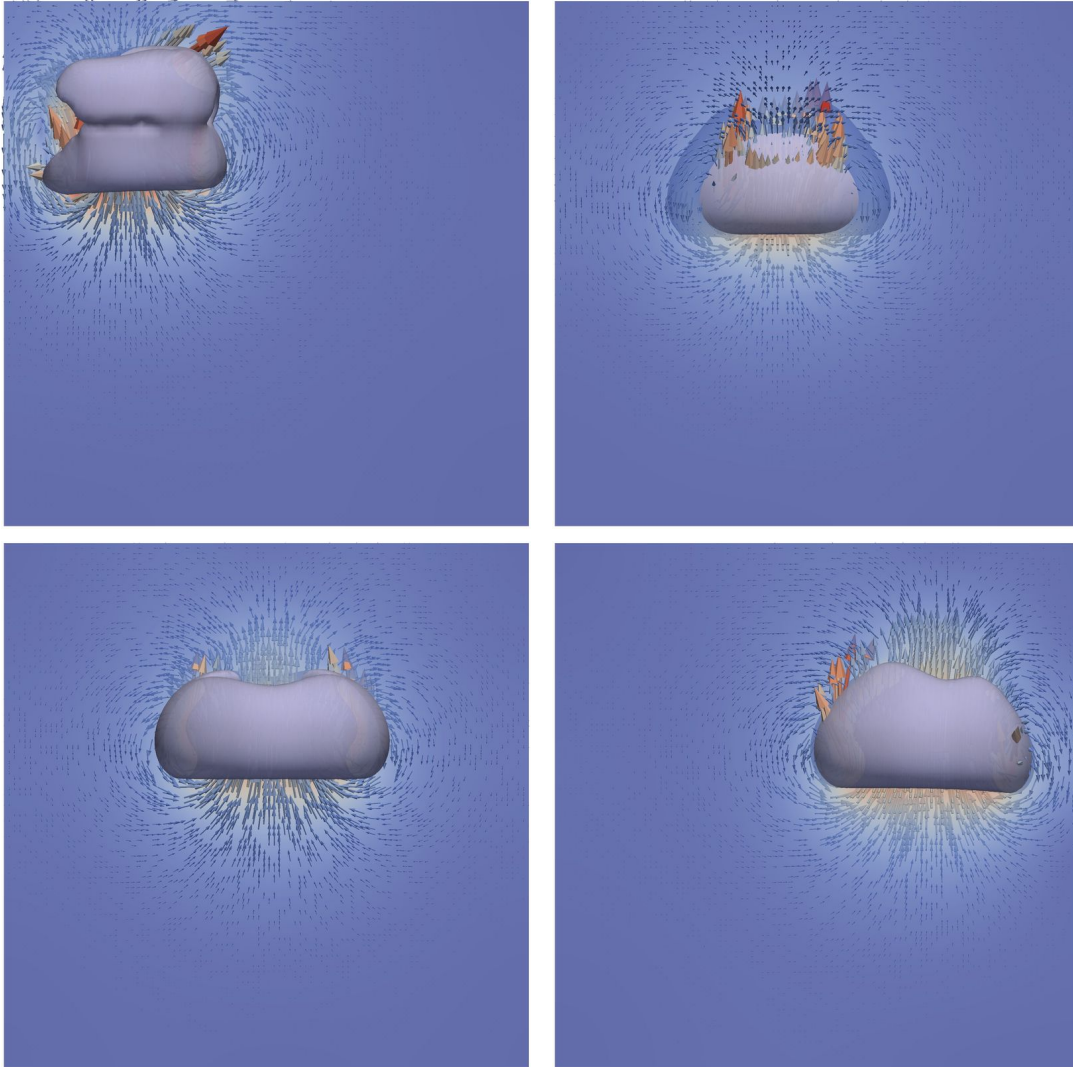
FIG. 8: Flow field and bubble visualization of solution realizations of the rising bubble problem with stochastic parameters $\mathbf{y}_8' \approx (0.05, 0.07, 0.12, 0.02, 863.64)^\top$, $\mathbf{y}_6' \approx (0.09, 0.05, 0.07, 0.09, 772.73)^\top$, $\mathbf{y}_{33}' \approx (0.1, 0.05, 0.12, 0.08, 512.4)^\top$, and $\mathbf{y}_{27}' \approx (0.14, 0.05, 0.09, 0.09, 735.54)^\top$ (from left to right)

For reason of simplicity, in contrast to the previous paragraphs, the subsequent convergence study compares kernel-based results and the Dakota-based sparse grid result using only the single-valued quantity of interest, $\mathbb{E}\big[c_2^h\big](T)$. The single deterministic two–phase flow problems are discretized and solved as before by using NaSt3DGPF. In the Dakota calculations, NaSt3DGPF is directly called from the Dakota control program.

We come back to the problem of a rising gas bubble in water which is subject to a random volume force; cf. Section 4.3. Again, the random input is modeled by a Karhunen–Loève expansion which is truncated after the third term; thus we have $D = 3$ stochastic dimensions and a correlation length of $L_c = 2.0$ is used. The quantity of interest is now the second component c_2^h of the bubble's center position at physical time $T = 0.2$ sec. The reference mean $\mathbb{E}\big[c_2^H\big](T)$ is approximated by a Gaussian kernel with $N_{\max} = 512$ collocation points. In the case of kernel-based approximation, the standard RBF norm $\| \cdot \| := \zeta \| \cdot \|_2$ with a modified scaling of $\zeta = 0.1$ is employed. Results computed with the Gaussian kernel are regularized with $\epsilon_{reg} = 10^{-6}$ while Matérn kernel results are regularized with $\epsilon_{reg} = 10^{-5}$. Quadrature is the full tensor-product quadrature on level $l_q = 9$.
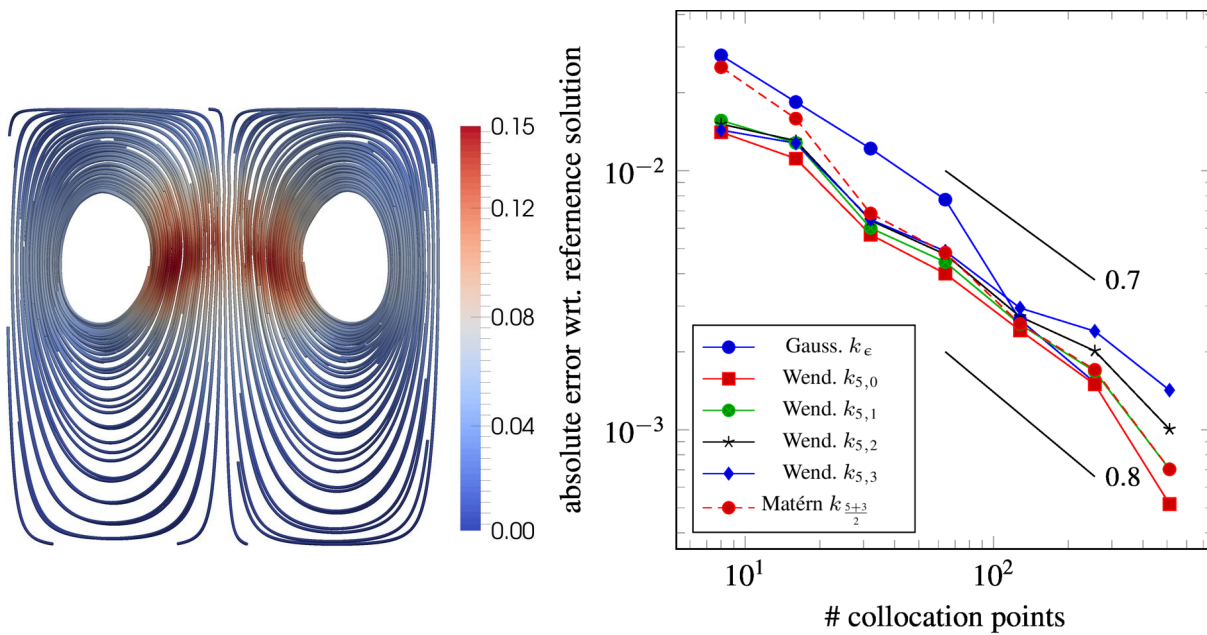
FIG. 9: Left: Streamline slice visualization of the mean velocity field (color-coded by velocity magnitude) in the bubble flow stochastic homogenization problem. Right: Error convergence results for the approximated mean of the first component of the velocity field $\mathbb{E}[U_1](T)$ of the same problem. Approximations using different kernel functions are compared.

In Fig. 10, convergence results are given for a mean approximation by Gaussian kernels, Matérn kernels, and stochastic collocation by sparse grids (SG). We observe that the kernel-based methods show better convergence
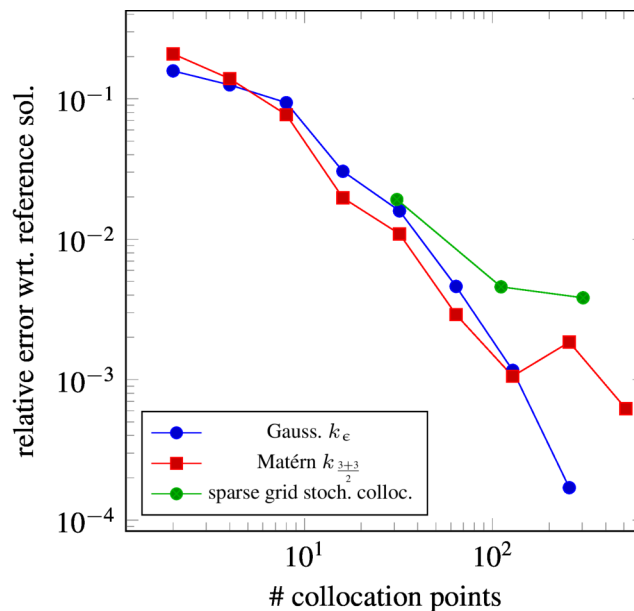

FIG. 10: Error convergence results of the approximation of the mean bubble center position $\mathbb{E}\left[c_2^h\right](T)$ in the large-scale two-phase flow problem with rising bubbles. Kernel-based stochastic collocation (with Gaussian and Matérn kernel) and sparse grid-based stochastic collocation are compared.

than the sparse grid method and a higher-order algebraic rate is achieved. Moreover, we even observe a spectral convergence rate for the Gaussian kernel. Furthermore, the errors of the RBF-based stochastic collocation method are always below the results of the sparse grid stochastic collocation method.

Note at this point that a computationally challenging problem is considered and to achieve an error with almost the size of 10^{-4} with only 256 simulations is quite remarkable. It is well known that stochastic collocation on sparse tensor-product constructions shows asymptotically exponential convergence rates on sufficiently smooth problems; see [6]. Nevertheless, in many large-scale uncertainty quantification application problems, the quantity of interest has limited smoothness with respect to the random input and/or bad preasymptotic error behavior is dominating the convergence to a significant extent. This is where kernel-based stochastic collocation has its main advantage.

5. CONCLUSIONS

In this work, the solution of random two-phase Navier–Stokes problems by means of the kernel-based stochastic collocation has been considered. Here, the first stochastic moment of solutions of two–phase flow problems was computed by applying a new *nonintrusive method* to the existing flow solver NaSt3DGPF which is based on a kernel approximation. For any method, given a fixed target error tolerance, it is indispensable to keep the number of discretization points in stochastic space as low as possible. A way to overcome this issue is to introduce an approximation method in stochastic space, which has high convergence order with a very small pre-asymptotic error. This has been achieved in this work by the introduction of the RBF kernel-based stochastic collocation method. Numerical results were given that underline the good properties of the kernel-based method. For the random two-phase Navier–Stokes equations, algebraic convergence rates were shown and a small error in the pre-asymptotic regime was always present. Thus, our kernel–based stochastic collocation approach outperformed well known established methods such as Monte Carlo, or sparse spectral tensor-product stochastic collocation in this situation.

REFERENCES

1. Ghanem, R. and Spanos, P., *Stochastic Finite Elements: A Spectral Approach*, New York: Springer-Verlag, 1991.

2. Schwab, C. and Gittelson, C., Sparse Tensor Discretizations of High-Dimensional Parametric and Stochastic PDEs, *Acta Numer.*, **20**:291–467, 5 2011.

3. Graham, I., Kuo, F., Nuyens, D., Scheichl, R., and Sloan, I., Quasi-Monte Carlo Methods for Elliptic PDEs with Random Coefficients and Applications, *J. Comput. Phys.*, **230**(10):3668–3694, 2011.

4. Barth, A., Schwab, C., and Zollinger, N., Multi-Level Monte Carlo Finite Element Method for Elliptic PDEs with Stochastic Coefficients, *Numer. Math.*, **119**(1):123–161, 2011.

5. Jakeman, J. and Roberts, S., Stochastic Galerkin and Collocation Methods for Quantifying Uncertainty in Differential Equations: a Review, *ANZIAM J.*, **50**:815–830, 2009.

6. Babuška, I., Nobile, F., and Tempone, R., A Stochastic Collocation Method for Elliptic Partial Differential Equations with Random Input Data, *SIAM Rev.*, **52**(2):317–355, 2010.

7. Ganis, B., Klie, H., Wheeler, M., Wildey, T., Yotov, I., and Zhang, D., Stochastic Collocation and Mixed Finite Elements for Flow in Porous Media, *Comput. Methods Appl. Mech. Eng.*, **197**(43-44):3547–3559, 2008.

8. Le Maître, O. and Knio, O., *Spectral Methods for Uncertainty Quantification: With Applications to Computational Fluid Dynamics*, Scientific Computation, Dordrecht: Springer, 2010.

9. Schick, M., Heuveline, V., and Le Maître, O., A Newton–Galerkin Method for Fluid Flow Exhibiting Uncertain Periodic Dynamics, *SIAM/ASA J. Uncertainty Quantif.*, **2**(1):153–173, 2014.

10. Croce, R., Griebel, M., and Schweitzer, M., Numerical Simulation of Bubble and Droplet-Deformation by a Level Set Approach with Surface Tension in Three Dimensions, *Int. J. Numer. Methods Fluids*, **62**(9):963–993, 2009.

11. Dornseifer, T., Griebel, M., and Neunhoeffer, T., *Numerical Simulation in Fluid Dynamics, a Practical Introduction*, Philadelphia: SIAM, 1998.

12. Burkow, M. and Griebel, M., A Full Three Dimensional Numerical Simulation of the Sediment Transport and the Scouring at a Rectangular Obstacle, *Comput. Fluids*, **125**:1–10, 2016.

13. Griebel, M. and Rüttgers, A., Multiscale Simulations of Three-Dimensional Viscoelastic Flows in a Square-Square Contraction, *J. non-Newtonian Fluid Mech.*, **205**:41–63, 2014.

14. Zaspel, P. and Griebel, M., Solving Incompressible Two-Phase Flows on Multi-GPU Clusters, *Comput. Fluids*, **80**:356–364, 2013.

15. Krige, D., A Statistical Approach to Some Basic Mine Valuation Problems on the Witwatersrand, *J. Chem. Metall. Mining Soc. S. Afr.*, **52**(6):119–139, 1951.

16. van Beers, W. and Kleijnen, J., Kriging Interpolation in Simulation: A Survey, in *Proc. of the Winter Simulation Conference 2004*, Vol. 1, pp. 113–121, 2004.

17. Rasmussen, C. and Williams, C., *Gaussian Processes for Machine Learning (Adaptive Computation and Machine Learning)*, Cambridge, MA: The MIT Press, 2005.

18. Cialenco, I., Fasshauer, G., and Ye, Q., Approximation of Stochastic Partial Differential Equations by a Kernel-Based Collocation Method, *Int. J. Comput. Math.*, **89**(18):2543–2561, 2012.

19. Fasshauer, G. and Ye, Q., A Kernel-Based Collocation Method for Elliptic Partial Differential Equations with Random Coefficients, in *Monte Carlo and Quasi-Monte Carlo Methods 2012*, J. Dick, F. Kuo, G. Peters, and I. Sloan, Eds., Springer Proceedings in Mathematics and Statistics, Berlin, Heidelberg: Springer, **65**:331–347, 2013.

20. Griebel, M. and Rieger, C., Reproducing Kernel Hilbert Spaces for Parametric Partial Differential Equations, *SIAM/ASA J. Uncertainty Quantif.*, **5**:111–137, 2017.

21. Zaspel, P., Parallel RBF Kernel-Based Stochastic Collocation for Large-Scale Random PDEs, PhD, University of Bonn, Germany, 2015.

22. Narcowich, F. and Ward, J., Scattered-Data Interpolation on $\mathbb{R}^n$: Error Estimates for Radial Basis and Band-Limited Functions, *SIAM J. Math. Anal.*, **36**(1):284–300, 2004.

23. Wendland, H., *Scattered Data Approximation*, Cambridge, UK: Cambridge University Press, 2004.

24. Sussman, M., Smereka, P., and Osher, S., A Level Set Approach for Computing Solutions to Incompressible Two-Phase Flow, *J. Comput. Phys.*, **114**:146–159, 1994.

25. Gross, S. and Reusken, A., *Numerical Methods for Two-Phase Incompressible Flows*, Springer Series in Computational Mathematics, Vol. 40, Berlin, Heidelberg: Springer, 2011.

26. Brackbill, J., Kothe, D., and Zemach, C., A Continuum Method for Modeling Surface Tension, *J. Comput. Phys.*, **100**(2):335–354, 1992.

27. Osher, S. and Sethian, J., Fronts Propagating with Curvature-Dependent Speed: Algorithms based on Hamilton-Jacobi Formulations, *J. Comput. Phys.*, **79**(1):12–49, 1988.

28. Chorin, A., Numerical Solution of the Navier-Stokes Equations, *Math. Comput.*, **22**(104):745–762, 1968.

29. Tikhonov, A. and Arsenin, V., *Solutions of Ill-Posed Problems*, Scripta Series in Mathematics, Silver Spring, MD: Winston, 1977.

30. Hansen, P.C., The Truncated SVD As a Method for Regularization, *BIT Numer. Math.*, **27**(4):534–553, 1987.

31. Caflisch, R., Monte Carlo and Quasi-Monte Carlo Methods, *Acta Numer.*, **7**:1–49, 1998.

32. Chi, H., Mascagni, M., and Warnock, T., On the Optimal Halton Sequence, *Math. Comput. Simul.*, **70**(1):9–21, 2005.

33. Leobacher, G. and Pillichshammer, F., *Introduction to Quasi-Monte Carlo Integration and Applications*, Compact Textbooks in Mathematics, Cham, Switzerland: Springer, 2014.

34. Wang, X. and Sloan, I.H., Low Discrepancy Sequences in High Dimensions: How Well Are Their Projections Distributed?, *J. Comput. Appl. Math.*, **213**(2):366–386, 2008.

35. Fasshauer, G., *Meshfree Approximation Methods with MATLAB*, Interdisciplinary Mathematical Sciences, World Scientific, 2007.

36. Tuminaro, R., Phipps, E., Miller, C., and Elman, H., Assessment of Collocation and Galerkin Approaches to Linear Diffusion Equations with Random Data, *Int. J. Uncertainty Quantif.*, **1**(1):19–33, 2011.

37. Davis, P. and Rabinowitz, P., *Methods of Numerical Integration, Computer Science and Applied Mathematics*, New York: Academic Press, 1984.

38. Adams, B., Bauman, L., Bohnhoff, W., Dalbey, K., Ebeida, M., Eddy, J., Eldred, M., Hough, P., Hu, K., Jakeman, J., Swiler, L., and Vigil, D., DAKOTA, A Multilevel Parallel Object-Oriented Framework for Design Optimization, parameter estimation, uncertainty quantification, and sensitivity analysis: Version 5.4 Theory Manual, Sandia National Lab, Sandia Tech. Rep. SAND2011-9106, 2009.

39. Nobile, F., Tempone, R., and Webster, C., An Anisotropic Sparse Grid Stochastic Collocation Method for Partial Differential Equations with Random Input Data, *SIAM J. Numer. Anal.*, **46**(5):2411–2442, 2008.

APPENDIX A. PARAMETERS FOR SPARSE GRID STOCHASTIC COLLOCATION

For the sake of reproducibility, we give here the Dakota settings, which are used in Section 4.5.

Configuration 1. Standard parameters for sparse grid stochastic collocation in Dakota

```
method
  stoch_collocation
    sparse_grid_level = <level>
    dimension_preference = <N_KL>*1
    samples = 10000 seed = 12347 rng rnum2
    output silent
```